Large-scale climate response to regionally confined extratropical cooling: Effect of ocean dynamics

Jiyeong Kim[1], Sarah M. Kang[2*], Shang-Ping Xie[3], Baoqiang Xiang[4,5], Doyeon Kim[2], Xiao-Tong Zheng[6], and Hai Wang[6]

[1]Operational Systems Development Department, National Institute of Meteorological Sciences, Seogwipo 63568, South Korea

[2]Department of Urban and Environmental engineering, Ulsan National institute of Science and Technology, Ulsan 44919, South Korea

[3]Scripps Institution of Oceanography, University of California San Diego, La Jolla, California 92093, USA

[4]NOAA/Geophysical Fluid Dynamics Laboratory, Princeton, New Jersey, 08540, USA

[5]University Corporation for Atmospheric Research, Boulder, Colorado 80307, USA

[6]Physical Oceanography Laboratory, Institute for Advanced Ocean Studies, Ocean University of China and Qingdao National Laboratory for Marine Science and Technology, Qingdao, China

Correspondence to: Sarah M. Kang (skang@unist.ac.kr), ORCID: 0000-0003-4635-275X

Abstract

This study investigates the effect of ocean dynamics on the tropical climate response to localized radiative cooling over three northern extratropical land regions using hierarchical model simulations that vary in the degree of ocean coupling. Without ocean dynamics, the tropical climate response is independent of the extratropical forcing location, characterized by a southward tropical precipitation shift with a high degree of zonal symmetry, a reduced zonal sea surface temperature (SST) gradient along the equatorial Pacific, and the eastward-shifted Walker circulation. When ocean dynamical adjustments are allowed, the zonal-mean tropical precipitation shift is damped primarily via Eulerian-mean ocean heat transport. The oceanic damping effect is strongest (weakest) for North Asian (American) cooling, associated with the largest (smallest) Eulerian-mean ocean heat transport across the equatorial Pacific. The cross-equatorial ocean heat transport in the Pacific is anchored to the North Pacific subtropical high, the response of which can be inferred from the corresponding slab ocean simulations. Hence, the slab ocean simulations provide useful a priori prediction for oceanic damping efficiency.

Ocean dynamics also modulates the spatial pattern of climate response in a distinct manner depending on the zonal distribution of imposed forcing. North Asian forcing induces a pronounced eastern equatorial Pacific cooling extending to the western basin, accompanying the westward shifted Walker circulation. European forcing causes cooling confined to the eastern equatorial Pacific and strengthens the Walker circulation. The tropical precipitation response in these two cases exhibits large zonal variations with a high degree of equatorial symmetry, being essentially uncorrelated with the corresponding slab ocean simulations. By contrast, North American forcing induces a sufficiently strong inter-hemispheric contrast in the tropical Pacific SST response, due to the relatively weak oceanic

damping effect, producing a weaker but spatially similar tropical response to that in the slab ocean simulation.

This study demonstrates that the effect of ocean dynamics in modulating the tropical climate response depends on the extratropical forcing location. The results are relevant for understanding the distinct climate response induced by aerosols from different continental sites.

Keywords

Tropical precipitation shifts, Walker circulation, High-latitude thermal forcing, Model hierarchy, Dynamic ocean

1. Introduction

Aerosols, together with greenhouse gases (GHG), are the major driver of global climate change. Aerosols perturb the radiation budget over the source regions by altering the solar radiation balance (i.e., direct effect) and by changing cloud microphysical properties (i.e., indirect effects). The locally perturbed radiation balance instigates large-scale atmospheric circulation changes that alter the tropical precipitation globally (Ming and Ramaswamy, 2009). As anthropogenic aerosols preferentially cool the Northern Hemisphere, the Hadley circulation responds in a way to transport anomalous heat northward across the equator, giving rise to a southward cross-equatorial moisture transport and a corresponding Inter-Tropical Convergence Zone (ITCZ) shift (Kang et al., 2008; Kang, 2020). This energetic constraint attributes the southward ITCZ shift in the late 20th century to anthropogenic aerosol forcing (Hwang et al., 2013; Wang et al., 2016).

The aerosol-induced tropical sea surface temperature (SST) and precipitation responses are shown to be remarkably similar in spatial pattern to the GHG-induced

responses with a reversed sign (Xie et al., 2013). This feature, however, is presumably relevant for the period prior to the late 1970s when aerosols increased concurrently over all major Northern Hemisphere continents. While the anthropogenic aerosols were thought to broadly counteract the climatic effect of greenhouse gases (Forster et al. 2007), it became more challenging to understand the aerosol-forced climate response as anthropogenic aerosol emissions undergo spatially and temporally complex variations (Deser et al., 2020; Kang et al., 2021; Diao et al., 2021). The regions of major aerosol emissions were the United States and Europe in the 1970s but shifted to Asia in the 1980s as a consequence of clean air act in the western hemisphere. Aerosol emissions within Asia have changed since about 2010, with a marked reduction in China and a concurrent increase in India (Samset et al., 2019). The role of the spatiotemporal evolution of aerosol forcing in modulating the historical climate change has attracted much recent attention (e.g., Deser et al., 2020; Hirasawa et al., 2020; Kang et al., 2021; Wang and Wen, 2021; Shi et al., 2022). Before the late 1970s, the aerosol-forced response is dominated by a predominant Northern Hemisphere cooling with a large zonal symmetry, whereas the aerosol-forced response since the late 1970s is characterized by large zonal variations between the North Pacific cooling and the North Atlantic warming with a negligible zonal-mean response. The former response is largely captured by the zonally uniform radiative cooling in the extratropics and the latter response by the zonally anti-symmetric forcing (i.e., cooling over the eastern hemisphere and heating over the western hemisphere). A transition from the dominance of zonally symmetric to anti-symmetric forcing effects broadly explains the evolving aerosol-forced tropical climate change in the historical period (Kang et al., 2021). However, the relative contributions from evolving aerosol forcing in different regions remain to be elucidated.

In motionless slab ocean models, which a large literature on aerosol-induced climate change is based on, the tropical precipitation response is remarkably similar spatially,

insensitive to the perturbed longitudes as long as the forcing is introduced in the extratropics (L'Hévéder et al., 2015; Kang et al., 2018a, 2021). By contrast, in fully coupled models, the extratropical forcing at different longitudes produce vastly different tropical precipitation responses (White et al., 2018). The role of ocean dynamics in modulating the tropical climate response pattern has been implied in recent studies. Ocean dynamics effectively damps the tropical precipitation response to zonally symmetric interhemispheric forcing (Deser et al., 2015; Kay et al., 2016; Hawcroft et al., 2017; Kang et al., 2018b), with an increasing oceanic damping effect for a higher-latitude forcing (Xiang et al., 2018; Green et al., 2019; Yu and Pritchard, 2019; Kang et al., 2019). In contrast to the robust oceanic role in dampening the effect of zonally symmetric extratropical forcing, the effect of zonally anti-symmetric extratropical forcing (i.e., eastern-hemisphere cooling and western-hemisphere warming) on the equatorial Pacific is shown to be amplified through Bjerknes feedback (Kang et al., 2021). Put together, different parts of ocean circulation come into play in shaping the tropical climate response depending on the forcing distribution. However, it has not been systematically examined how ocean dynamics modulates the effect of zonally confined extratropical forcing by comparing the model with and without a dynamic ocean. Any given localized forcing consists of the zonally symmetric and anti-symmetric components, with the former effect muted and the latter effect amplified by ocean dynamics. The relative contribution of the two components to determining the total climate response may depend on the forcing longitude, for example, according to whether the given forcing is more prone to perturbing the Pacific subtropical cell or Atlantic Meridional Overturning Circulation (AMOC). That is, one may hypothesize that the tropical climate response is sensitive to the extratropical forcing distribution in fully coupled model experiments, in stark contrast to the conclusion drawn from previous slab ocean model experiments.

Thus, we aim to assess the sensitivity of the large-scale tropical climate response to the longitudinal location of extratropical radiative forcing using a hierarchy of model configurations that varies in the degree of ocean coupling. While ocean dynamical impacts from extratropical aerosol radiative forcings are exerted on the high-latitudes as well (Wang et al. 2018), we focus on the tropical response in this study. To sidestep large uncertainties in the radiative forcing associated with anthropogenic aerosol emissions, we reduce insolation over a finite region instead of perturbing aerosol emissions, following the approach in Kang et al. (2021). Not meant to be realistic, this approach allows us to cleanly isolate the effect of a varying forcing location by fixing the forcing magnitude. This strategy of reducing insolation is often taken in idealized geoengineering simulations to represent sulfate aerosols (e.g., Tilmes et al., 2013). A better understanding of how the climate response to regional radiative forcing depends on the forcing location will allow us to establish a more reliable projection of aerosol-forced climate response.

This paper is organized as follows. Section 2 introduces model and experimental design. Section 3 discusses the zonal mean precipitation response in relation to the energetic constraints, with a detailed examination of the top-of-atmosphere (TOA) radiation budget and cross-equatorial ocean heat transport. Section 4 examines how ocean dynamics modulate the spatial pattern of surface temperature and precipitation responses by comparing the slab and full ocean configurations. Finally, in section 5, we summarize the major findings in this study.

2. Model and experimental design

We use one version of Geophysical Fluid Dynamics Laboratory (GFDL) AM4 (Zhao et al., 2018) coupled to GFDL Forecast-Oriented Low Ocean Resolution (FLOR) (Vecchi et al., 2014). The atmospheric model has a horizontal resolution of 1° latitude x 1.25° longitude

with 32 vertical levels and the oceanic model has an approximate horizontal grid spacing of 1° with 50 vertical levels. We refer to this fully atmosphere-ocean coupled model setup as DOM (dynamic ocean model).

The control experiment is integrated for 200 years from a fully spun-up preindustrial run (DOM-CTRL). The control climatology is obtained by taking the last 170-yr mean. The three perturbation experiments are integrated starting from the same date as in DOM-CTRL for 100 years after an abrupt reduction of insolation over three different extratropical land regions. Although 100 years is not enough for the deep ocean to equilibrate, the transition into a new quasi-equilibrium state takes place after 30 years based on a small global imbalance of TOA radiation in the order of 0.1 W m^{-2}. Hence, we analyse the average over the last 70 years, which is a sufficiently long period to reduce the effect of internal variability. The insolation is reduced between 45°N-65°N over a 65° longitudinal extent, representing aerosol cooling over North Asia (70°E-135°E; DOM-NASIA), North America (60°W-125°W; DOM-NAMER), and Europe (0°E-65°E; DOM-EURO). The area-integrated forcing amounts to -0.4 PW in all cases, equivalent to 67 W m^{-2} when averaged over the forcing domain. We perturb the system with a forcing considerably stronger than the aerosol-induced net radiation response, which is on the order of 10 W m^{-2} at a regional scale (Wang et al., 2015), in order to cleanly separate forced responses from internal climate variability. It is implicitly assumed that the response is linear in the forcing magnitude, the sensitivity to which warrants further investigation. Additionally, for an easy comparison across the experiments, we set the forced latitude to 45°N-65°N for all cases, which is approximately the latitudinal range of actual aerosol forcing over Europe. This latitudinal range, however, is higher than the actual aerosol emission regions in Asia and North America. We take this strategy to isolate the effect of longitudinal variations of regionally confined extratropical

radiative forcing. A future study is planned to perturb the Asian region at lower latitudes for greater realism.

To examine the role of ocean dynamics, we perform the same experiments with the atmospheric model AM4 coupled with a 50 m slab ocean model. We refer to this slab ocean model setup as SOM. The control simulation (SOM-CTRL) is run with the q-flux that aims to reproduce the climatological SST distribution from DOM-CTRL. The SOM-CTRL is perturbed by the regional radiative perturbations identical to the DOM experiments (i.e., SOM-NASIA, SOM-NAMER, and SOM-EURO). All SOM experiments are integrated for 100 years and the annual-means for the last 70 years are analysed to exclude the initial adjustment period. We denote the climatology difference between the perturbed and control experiments by Δ.

3. Energetics and zonal mean response

We begin by comparing the tropical climate responses to the three forcing locations in the zonal-mean context. The zonally averaged surface temperature response is largely independent of forcing location equatorward of 50° for both SOM and DOM configurations (Fig. 1a). Consistent with the zonal-mean surface temperature response, the zonal-mean precipitation responses for the SOM experiments exhibit little sensitivity to the forcing location, with the spatial correlation at 0.99 between 30°S and 30°N. By contrast, in the presence of a dynamic ocean, the zonal-mean precipitation responses are spatially distinct depending on the extratropical forcing location, with only weakly correlated among the DOM experiments, ranging from 0.33 to 0.58. In this section, we invoke the energetics framework to understand the sensitivity of zonally averaged tropical precipitation response to the forcing location.

The zonal-mean tropical precipitation response is linked to the cross-equatorial atmospheric energy transport response $\Delta\mathrm{AHT}_0$ (e.g., Kang, 2020), with a southward tropical precipitation shift corresponding to a northward $\Delta\mathrm{AHT}_0$ (Fig. 2). The atmospheric energy budget in a quasi-equilibrium state, in which the energy tendency in the atmospheric column can be neglected, gives:

$$\Delta\mathrm{AHT}_0 = \langle \Delta R_{\mathrm{TOA}} \rangle - \langle \Delta\mathrm{OHU} \rangle \quad (1)$$

where R_{TOA} is the net downward top-of-atmosphere (TOA) radiation and OHU the ocean heat uptake, calculated as net downward surface heat flux. Brackets denote the spatial integral in the Southern Hemisphere minus that in the Northern Hemisphere divided by 2, indicative of a cross-equatorial flux in the unit of PW. The net TOA radiation response ΔR_{TOA} includes the prescribed solar flux perturbation $\Delta S^{\downarrow}$, only a fraction of which is felt by the climate system due to the planetary albedo. We may define the prescribed forcing as $R_{\mathrm{S}} = (1-\alpha)\Delta S^{\downarrow}$ where α is the planetary albedo averaged between the control and perturbed experiments. Defining $\Delta R_{\mathrm{TOA-S}}$ as the difference between the net downward TOA radiation response ΔR_{TOA} and the prescribed forcing R_{S} allows us to rearrange Eq. (1) as:

$$1 = \frac{\Delta\mathrm{AHT}_0}{\langle R_{\mathrm{S}} \rangle} + \frac{\langle -\Delta R_{\mathrm{TOA-S}} \rangle}{\langle R_{\mathrm{S}} \rangle} + \frac{\langle \Delta\mathrm{OHU} \rangle}{\langle R_{\mathrm{S}} \rangle}$$

where the terms on the right-hand-side represent the atmospheric compensation C_{ATM}, TOA compensation C_{TOA}, and oceanic compensation C_{OCN}, respectively (Kang et al., 2019).

Figure 3 compares the fractional compensation by each component in all experiments. In SOM with no ocean dynamics (Fig. 3a), the forcing is mostly compensated by the atmospheric energy transport (C_{ATM} = 93.2±5.7 %) with some contribution from the TOA radiation (C_{TOA}= 12.7±5.4 %). The oceanic compensation C_{OCN} is negligible in the slab ocean setting but non-zero due to surface heat flux change on the ice edges. The relative contribution of each component in balancing the forcing is fairly insensitive to the forcing

location. With active ocean dynamics (Fig. 3b), the TOA compensation C_{TOA} stays similar to that in the SOM while the oceanic compensation C_{OCN} takes over a considerable fraction of the atmospheric compensation C_{ATM}, effectively dampening the zonal-mean tropical precipitation shift in DOM (Fig. 2). Next, we examine the TOA radiation response and the ocean heat budget in more detail.

3.1. TOA radiation response

In order to examine what sets the TOA compensation, we divide C_{TOA} into the contributions from the extratropics (i.e., $\langle -\Delta R_{\mathrm{TOA-S}} \rangle$ poleward of 30°S/N; Fig. 4a) and the tropics (i.e., $\langle -\Delta R_{\mathrm{TOA-S}} \rangle$ equatorward of 30°S/N; Fig. 4b). We further attribute the regional C_{TOA} to the clear-sky longwave radiation response (ΔL_{clr}), longwave cloud radiative effect response (ΔL_{cre}; the TOA longwave flux in all-sky minus clear-sky), and shortwave radiation response due to changes in cloud (ΔS_{cld}), non-cloud atmospheric constituents (ΔS_{ncld}), and surface albedo (ΔS_{alb}). The shortwave terms are separated by the Approximate Partial Radiative Perturbation (APRP) method (Taylor et al., 2007; Kim et al. 2022). The C_{TOA} decomposition results for the SOM experiments are shown in Fig. 4. The positive values indicate a compensating effect (i.e., negative feedback) and the negative values indicate an amplifying effect (i.e., positive feedback).

On average, the TOA radiation response in the extratropics offsets the forcing by 38.6 % while that in the tropics acts to amplify the forcing by 25.9 %, giving the net C_{TOA} of 12.7 %. In the extratropics, the compensating effect results from the reduction in clear-sky outgoing longwave radiation associated with the northern extratropical cooling, about half of which is cancelled by the positive feedback from the shortwave radiation (Fig. 4a). The shortwave-induced positive feedback arises from the increase in low cloud amount (ΔS_{cld}), reduction in shortwave absorption by water vapor (ΔS_{ncld}), and increase in surface albedo

(ΔS_{alb}). In the tropics, the positive TOA feedback results from the increase in clear-sky outgoing longwave radiation in the northern tropics as the ITCZ shifts southward (Clark et al. 2018) whereas the cloud radiative effects feature little hemispheric asymmetry due to the cancellation between the longwave and shortwave components (Fig. 4b).

With interactive ocean dynamics, the negative TOA feedback in the extratropics is damped (cross symbols in Fig. 4a) as a consequence of weaker temperature responses and the positive TOA feedback in the tropics (cross symbols in Fig. 4b) is also damped associated with a muted ITCZ shift. As a result, the TOA compensation is nearly independent of the degree of atmosphere-ocean coupling (Fig. 3).

3.2. Oceanic compensation

The zonally- and vertically-integrated oceanic heat budget indicates that the ocean heat uptake OHU consists of the ocean heat storage OHS and ocean heat transport divergence $\nabla \cdot$ OHT:

$$\mathrm{OHU} = \mathrm{OHS} + \nabla \cdot \mathrm{OHT}$$

with $\mathrm{OHT} = \int_{-H}^{0} \rho_o C_p v\theta \,\mathrm{dz}$ and $\mathrm{OHS} = \frac{\partial}{\partial t}\int_{-H}^{0} \rho_o C_p \theta \,\mathrm{dz}$ (i.e., the ocean heat content tendency), where v is the velocity, ρ_o is the seawater density, C_p is the specific heat of seawater, θ is the potential temperature, and $-H$ denotes the ocean depth. We calculate OHS by the linear trend of ocean heat content over the 70-year period at each grid point. We use the direct model output of Eulerian-mean ocean heat transport $\mathrm{OHT}_{\mathrm{Eul}} = \int_{-H}^{0} \rho_o C_p \bar{v}\bar{\theta} \,\mathrm{dz}$ where the overbar denotes the time average, and consider the residual $\nabla \cdot \mathrm{OHT}_{\mathrm{res}} = \mathrm{OHU} - \mathrm{OHS} - \nabla \cdot \mathrm{OHT}_{\mathrm{Eul}}$ as the ocean heat transport divergence by eddies and diffusion. Hence, the oceanic compensation C_{OCN} (i.e., $\langle \Delta\mathrm{OHU} \rangle / \langle R_{\mathrm{S}} \rangle$) can be induced by changes in ocean heat storage $\langle \Delta\mathrm{OHS} \rangle$, cross-equatorial ocean heat transport by Eulerian-mean flow $\Delta\mathrm{OHT}_{\mathrm{Eul0}}$, and the residual, as compared in Fig. 5 for the DOM experiments.

The oceanic compensation can be largely attributed to the anomalously northward Eulerian-mean ocean heat transport across the equator $\Delta \mathrm{OHT}_{\mathrm{Eul0}}$ with relatively small contributions from anomalous ocean heat storage and residual. That is, $\Delta \mathrm{OHT}_{\mathrm{Eul0}}$ is responsible for the sensitivity in oceanic compensation to the forcing location. We further decompose $\Delta \mathrm{OHT}_{\mathrm{Eul0}}$ into contributions from each basin. The DOM-NASIA and DOM-EURO cases induce a substantial $\Delta \mathrm{OHT}_{\mathrm{Eul0}}$ over both Indo-Pacific and Atlantic basins while the DOM-NAMER case is primarily balanced from the Atlantic with a negligible contribution from the Indo-Pacific basin. The contrasting $\Delta \mathrm{OHT}_{\mathrm{Eul0}}$ by basin can be understood from the distinct response of the ocean meridional overturning circulation (Fig. 6). The AMOC strengthens regardless of the forcing location as the air temperature response is effectively homogenized by atmospheric eddies and mean westerlies, making the surface ocean density over the Labrador Sea denser, thereby enhancing the deep water formation. However, the extent to which the AMOC strengthens is weakest in DOM-NASIA (Fig. 6, left), presumably due to the distance between the forcing region and the Atlantic basin, corresponding to the smallest $\Delta \mathrm{OHT}_{\mathrm{Eul0}}$ in the Atlantic basin (i.e., $\Delta \mathrm{OHT}_{\mathrm{Eul0}}^{\mathrm{Atl}}$ in Fig. 5).

The Indo-Pacific $\Delta \mathrm{OHT}_{\mathrm{Eul0}}$ changes in proportion to the North Pacific subtropical cell response, which in turn is anchored to the North Pacific Subtropical High. That is, the North Pacific subtropical cell strengthens in association with the amplified North Pacific Subtropical High and vice versa. The sea level pressure response is characterized by a surface high east of the forcing domain and a surface low west of the forcing domain in order to balance the prescribed extratropical cooling by meridional warm advection (Hoskins and Karoly 1981). Consequently, the North Pacific Subtropical High strengthens in response to NASIA forcing (Fig. 7a,d) while weakening in response to NAMER forcing (Fig. 7b,e). The EURO forcing gives rise to a weak strengthening of the North Pacific Subtropical High (Fig. 7c,f). As a result, the North Pacific subtropical cell most effectively strengthens in DOM-

NASIA (Fig. 6d), giving rise to the largest $\Delta\mathrm{OHT}_{\mathrm{Eul0}}$ in the Indo-Pacific basin (i.e., $\Delta\mathrm{OHT}_{\mathrm{Eul0}}^{\mathrm{Ind-Pac}}$ in Fig. 5). A modest strengthening of North Pacific subtropical cell in DOM-EURO (Fig. 6f) results in a smaller $\Delta\mathrm{OHT}_{\mathrm{Eul0}}^{\mathrm{Ind-Pac}}$ than in DOM-NASIA (Fig. 5). In DOM-NAMER, low pressure anomaly in the North Pacific extends to the western basin of the tropical Pacific whereas the eastern basin exhibits minimal high pressure anomaly as the Atlantic cold SST anomaly reaches the northeastern tropical Pacific across the Central American Isthmus (Fig. 7b,e). As a result, the NAMER forcing has little impact on the North Pacific subtropical cell (Fig. 6e), causing negligible $\Delta\mathrm{OHT}_{\mathrm{Eul0}}^{\mathrm{Ind-Pac}}$ (Fig. 5). Consequently, the oceanic compensation C_{OCN} is smallest in DOM-NAMER, leading to the largest atmospheric compensation C_{ATM} (Fig. 3b) and thereby the strongest zonal-mean ITCZ shift (Fig. 2).

It is worth noting that the sea level pressure anomaly pattern is broadly insensitive to ocean dynamical adjustment (contrast left and right columns to Fig. 7). The sea level pressure anomaly patterns between the SOM and DOM configurations are correlated at 0.74, 0.77, and 0.63 for NASIA, NAMER, and EURO cases, respectively. Hence, the effectiveness of oceanic compensation in the Indo-Pacific basin $\Delta\mathrm{OHT}_{\mathrm{Eul0}}^{\mathrm{Ind-Pac}}$ can be crudely predicted from the corresponding SOM experiments. Considering the large area of the Indo-Pacific basin, $\Delta\mathrm{OHT}_{\mathrm{Eul0}}^{\mathrm{Ind-Pac}}$ is an important fraction of overall oceanic damping effect, which ultimately determines the extent to which zonal-mean tropical precipitation shifts are muted by a dynamic ocean.

4. Zonally asymmetric climate response

In order to understand the pattern formation mechanism of tropical SST response, we consider the mixed layer energy budget in the quasi-equilibrium state (Hwang et al. 2017):

$$\Delta Q_{\mathrm{SW}} + \Delta Q_{\mathrm{LW}} - \Delta Q_{\mathrm{LH}} - \Delta Q_{\mathrm{SH}} = \Delta\mathrm{OHU}$$

296 which states that net downward surface heat flux changes, which consist of net shortwave
297 radiation changes ΔQ_{SW}, net longwave radiation changes ΔQ_{LW}, latent heat flux changes
298 ΔQ_{LH}, and sensible heat flux changes ΔQ_{SH}, are balanced by the ocean heat uptake changes
299 ΔOHU, representative of the changes in ocean heat transport divergence. Using the bulk
300 formula for evaporation, the latent heat flux changes related with Newtonian cooling can be
301 expressed as $\Delta Q_{\mathrm{LH},T} = \alpha \bar{Q}_{\mathrm{LH}} \Delta T$ where $\alpha \equiv L_{\mathrm{v}}/(R_{\mathrm{v}}\bar{T}^2)$, with L_{v} the latent heat of
302 vaporization, R_{v} the gas constant for moist air, T the SST, and overbars denoting the control
303 climatology. The remainder $\Delta Q_{\mathrm{LH,others}} \equiv \Delta Q_{\mathrm{LH}} - \Delta Q_{\mathrm{LH},T}$, consists of latent heat flux
304 changes due to changes in wind speed, relative humidity, and stability. Then, we may
305 rearrange the equation for SST anomalies as

306 $$\Delta T = \frac{\Delta Q_{\mathrm{SW}} + \Delta Q_{\mathrm{LW}} - \Delta Q_{\mathrm{LH,others}} - \Delta Q_{\mathrm{SH}} - \Delta \mathrm{OHU}}{\alpha \bar{Q}_{\mathrm{LH}}} = \Delta T_{\mathrm{SW}} + \Delta T_{\mathrm{LW}} + \Delta T_{\mathrm{LH}} + \Delta T_{\mathrm{SH}} + \Delta T_{\mathrm{OHU}}. \quad (2)$$

307 The actual SST responses (shading in Fig. 8a-c for SOM experiments and in Fig. 9a-c for
308 DOM experiments) are closely approximated by the linear sum of the five terms (solid
309 contours in the corresponding figures). This verifies the applicability of Eq. (2) for
310 diagnosing the drivers of the tropical SST response pattern.
311
312 **4.1. Slab ocean model (SOM) experiments**
313 The global spatial pattern of surface temperature anomaly is shown in the left column of Fig.
314 7 for the SOM experiments. The forcing domain cools by a comparable magnitude of 5.43 K,
315 5.68 K, and 5.00 K in NASIA, NAMER, and EURO, respectively. While the surface cooling
316 response is most pronounced in the vicinity of the forcing domain, the overall surface
317 temperature response exhibits a large similarity in spatial pattern, consistent with Kang et al.,
318 (2018a). Not only the zonally averaged response is nearly indistinguishable among the
319 experiments (Fig. 1a) but also the pattern correlation of two-dimensional SST response
320 between 30°S-30°N amounts up to 0.97 as compared with -0.01 for the prescribed insolation

perturbation (Table 1 and Fig. 8a-c). The surface temperature response for all SOM experiments can be characterized by a large inter-hemispheric contrast with an extensive Northern Hemisphere cooling, as the extratropical temperature response is highly homogenized in the zonal direction due to mean advection and eddies before reaching the tropics (Kang et al., 2014, 2018a). Consistent with the similar spatial distribution of SST response among the SOM experiments, the zonally averaged precipitation response is essentially independent of the forcing location (Fig. 1b) and the two-dimensional precipitation response between 30°S-30°N is correlated in space at as strong as 0.86 (Table 1).

The major components for shaping the tropical SST response pattern are those associated with $\Delta Q_{\mathrm{LH,others}}$ (Fig. 8d-f) and ΔQ_{SW} (Fig. 8g-i). The tropical SST response is, to first order, governed by the wind-evaporation-SST (WES) feedback (Xie and Philander 1994), as implied by a pronounced SST cooling north of the equator associated with intensified surface winds and a weak SST warming south of the equator associated with reduced surface winds (Fig. 8d-f). The spatial anomalies of SST and scalar surface wind are correlated in the global tropics at -0.57, -0.56, and -0.47 for NASIA, NAMER, and EURO, respectively. Anomalous northerlies in the tropics are a surface manifestation of the cross-equatorial anomalous Hadley cell that results from the necessity of an anomalously northward cross-equatorial atmospheric energy transport for balancing the Northern Hemisphere insolation reduction. The WES-induced SST response ΔT_{LH} (Fig. 8d-f) is offset by the SST response due to net shortwave radiation changes ΔT_{SW} (Fig. 8g-i). Net shortwave radiation response in the tropics is concomitant with the precipitation response (contrast shading and contours in Fig. 8g-i), suggestive of the dominance of the cloud-sky component. Anti-correlation between ΔT_{LH} and ΔT_{SW} arises because negative ΔT_{LH} causes precipitation reduction that leads to positive ΔT_{SW} whereas positive ΔT_{LH} causes precipitation increase that

346 leads to negative ΔT_{SW}. Enhanced deep convection along the South Pacific Convergence
347 Zone (SPCZ) produces a cooling patch tilted southeastward extending from the western
348 equatorial Pacific (Fig. 8g-i). As a result, the zonal SST gradient across the equatorial Pacific
349 is reduced (Fig. 10a), leading to an eastward shift of deep convection regardless of the
350 forcing location (Fig. 10b-d).
351
352 **4.2. Dynamic ocean model (DOM) experiments**
353 The global spatial pattern of surface temperature anomaly is shown in the right column of
354 Fig. 7 for the DOM experiments. The forcing domain cools by 4.74 K, 4.65 K, and 3.72 K in
355 NASIA, NAMER, and EURO, respectively, equivalent to a 20 % reduction compared to the
356 corresponding SOM experiments. Because the oceanic damping effect is more evident in the
357 SST response, the zonal-mean surface temperature response is damped by about 40 % in
358 NASIA and NAMER compared to the SOM configuration (Fig. 1a). In DOM-EURO, the
359 zonal-mean surface temperature response poleward of 65°N is considerably muted (Fig. 1a),
360 associated with a substantial warming over the Barents-Kara Sea (Fig. 7f), which we plan to
361 address in the future study. In all cases, the northern extratropics are extensively cooled,
362 except over the subpolar North Atlantic (Fig. 7, right), wherein a warm blob appears as a
363 consequence of the strengthened AMOC (Fig. 6, left). The surface temperature response
364 away from the Arctic is particularly similar in response to NASIA and EURO forcings even
365 when dynamic ocean adjustments are allowed. The spatial correlation between 30°S-30°N
366 reaches 0.61 considering both ocean and land grids and 0.57 for the ocean only (Table 1).
367 The tropical SST response in DOM-NASIA and DOM-EURO commonly features a
368 southwest tilted strip of cold anomaly in the subtropical North Pacific, cold anomalies
369 centered on the equatorial Pacific, and weak tropical Atlantic response (Fig. 7d,f). In contrast,
370 DOM-NAMER exhibits a relatively strong inter-hemispheric contrast in the tropical SST

response over the Pacific and Atlantic basins (Fig. 7e), hence, only weakly correlated with the other two cases (Table 1).

Unlike the SOM experiments where the WES feedback largely governs the tropical SST response pattern, in the DOM experiments it is substantially modulated by the ocean heat uptake response ΔOHU (Fig. 9j-l) in addition to $\Delta Q_{\mathrm{LH,others}}$ (Fig. 9d-f) and ΔQ_{SW} (Fig. 9g-i). A considerable ΔOHU-induced cooling exists on the equatorial and southeastern Pacific in DOM-NASIA and DOM-EURO, while DOM-NAMER exhibits little ΔOHU to the south of the equator. Because the WES-feedback induced cooling is more prominent in the northern tropics, a combined effect of ΔOHU and $\Delta Q_{\mathrm{LH,others}}$ leads to the tropical SST response with a relatively strong inter-hemispheric contrast in DOM-NAMER and with a high degree of equatorial symmetry in DOM-NASIA and DOM-EURO. In DOM-NASIA, a strong intensification of the North Pacific Subtropical High (Fig. 7d) gives rise to anomalous northeasterlies in the tropical North Pacific (Fig. 9d). The resulting equatorial divergence via the strengthened North Pacific subtropical cell (Fig. 6d) causes cooling along the equatorial Pacific (Fig. 9j). Associated with the ΔOHU-induced cooling maximum in the western basin is the ΔSW-induced warming due to reduced deep convective activities (Fig. 9g), indicative of a westward shift of the rising branch of the Walker circulation (Fig. 10f). In DOM-EURO, strong anomalous northerlies in the eastern equatorial to the southeastern Pacific causes cooling via Ekman divergence whereas anomalous westerlies in the western equatorial Pacific causes warming via Ekman convergence (Fig. 9f,l). Consequently, the Walker circulation strengthens (Fig. 10h), suggested by a negative ΔT_{SW} (i.e., precipitation increase) in the western equatorial Pacific and a positive ΔT_{SW} (i.e., precipitation decrease) in the central-to-eastern equatorial Pacific (Fig. 9i). In DOM-NAMER, the inter-hemispheric gradient set by the WES feedback is partially offset by ΔT_{SW} (Fig. 9e,h), as in the SOM configuration. The eastern equatorial Pacific cooling is further amplified due to enhanced

upwelling while the central equatorial Pacific cooling is damped by dynamic ocean effects (Fig. 9k). Net result shows a small reduction in the zonal SST gradient from the western Pacific warm pool to the central Pacific (Fig. 10e), accompanying a slightly weakened Walker circulation (Fig. 10g).

4.3. Comparison between SOM and DOM experiments

In this section, we contrast the SOM and DOM experiments to better understand the effect of ocean dynamical adjustment. While ocean dynamics tend to damp the surface temperature response, the equatorial Pacific SST response is amplified and the zonal gradient is even reversed through Bjerknes feedback (contrast Fig. 10a,e; Kang et al. 2021). The SOM experiments are largely independent of the forcing region, with a clear inter-hemispheric gradient in the tropical SST response, a southward shift in the tropical precipitation, intensified equatorial trade winds, and a reduced zonal SST gradient in the equatorial Pacific (Figs. 1, 8, and 10). However, ocean dynamics introduce a large sensitivity of the climate response pattern to the forcing location (Table 1). It is worth noting that the sea level pressure anomaly pattern is largely unchanged as ocean dynamical adjustment is allowed (contrast left and right in Fig. 7).

In response to NAMER forcing, with active ocean dynamics, the northward ocean heat transport increases associated with the strengthened AMOC (Fig. 6b), dampening the anomalous cooling throughout the northern extratropics including the North Pacific (Fig. 7b,e), despite negligible changes in the North Pacific subtropical cell (Fig. 6e). Although the surface temperature response is weaker in DOM-NAMER than in SOM-NAMER, the spatial distribution of climate responses stays broadly similar. Notably, the two-dimensional SST responses between 30°S-30°N are correlated in space at 0.83 (Table 1). Furthermore, a fairly high spatial correlation of 0.52 is found in the tropical precipitation responses (Table 1),

421 which can be characterized by an overall southward shift in both DOM-NAMER and SOM-
422 NAMER, albeit weaker in magnitude in the presence of a dynamic ocean (Fig. 1b).
423 By contrast, in response to NASIA and EURO forcings, a dynamic ocean not only
424 damps the magnitude of global cooling response but also considerably alters the spatial
425 pattern of tropical climate responses. In the tropics, the surface temperature response is
426 spatially correlated between the SOM and DOM experiments at 0.61 in NASIA and 0.60 in
427 EURO, lower than in NAMER (Table 1). The tropical precipitation response is essentially
428 uncorrelated between the SOM and DOM experiments in NASIA and EURO (Table 1).
429 While the SOM experiments are characterized by a southward tropical precipitation shift, the
430 DOM experiments show considerable zonal variations in the tropical precipitation response
431 with a high degree of equatorial symmetry (Fig. 8g,I vs Fig. 9g,i).
432
433 **5. Summary**
434 In this study, we have examined the role of ocean dynamics in modulating the tropical
435 climate response to regional radiative cooling, by comparing the results with a motionless
436 (SOM) and fully dynamic (DOM) ocean. Insolation is reduced over three extratropical land
437 regions (North Asia, North America, and Europe) to mimic aerosol forcing. A preferential
438 Northern Hemisphere cooling induces a southward shift of the zonal-mean ITCZ, but is
439 effectively damped in the presence of a dynamical ocean, as shown in many other studies
440 (Deser et al., 2015; Kay et al., 2016; Hawcroft et al., 2017; Xiang et al., 2018; Kang et al.,
441 2018b; Yu and Pritchard, 2019). We further find that the effect of oceanic modulation
442 depends on the forcing location according to anomalous high pressure to the east and
443 anomalous low pressure to the west of the land region the radiative cooling is applied to
444 (Hoskins and Karoly 1981). The regional radiative cooling accompanying a stronger North
445 Pacific Subtropical High would strengthen the North Pacific subtropical cell, leading to a

446 large oceanic compensation in the Indo-Pacific basin, suggestive of strongly damped zonal-
447 mean ITCZ shifts. This is the case for radiative cooling over North Asia and Europe. By
448 contrast, North American cooling induces anomalous low pressure in the North Pacific,
449 limiting the oceanic compensation in the Indo-Pacific basin. A relatively weaker oceanic
450 compensation leads to the atmospheric compensation and the zonal-mean ITCZ shift more
451 than double that in other two cases. Given that the sea level pressure response stays similar
452 between the SOM and DOM configurations, the SOM experiments provide useful a priori
453 predictions for oceanic damping efficiency.

454 Apart from the oceanic compensation, the energetics framework indicates that the
455 TOA radiation response also affects the zonal-mean ITCZ response. Separating the TOA
456 radiation response in the extratropical and the tropical regions allows us to find that the
457 compensating effect from the extratropics is partially offset by an amplifying effect from the
458 tropics, both of which is dominated by the clear-sky longwave radiation component. The
459 negative TOA feedback in the extratropics results from the reduced clear-sky outgoing
460 longwave radiation due to the northern extratropical cooling. The positive TOA feedback in
461 the tropics results from the enhanced clear-sky outgoing longwave radiation in the northern
462 tropics as the ITCZ shifts away to the south. Dynamic ocean adjustments weaken both the
463 negative extratropical and positive tropical feedbacks, associated with damped temperature
464 response and weaker ITCZ shifts, resulting in a radiative compensation fairly similar between
465 SOM and DOM configurations.

466 We further address how ocean dynamical effects alter the spatial pattern of climate
467 response. While the tropical climate response pattern is broadly insensitive to the forcing
468 region in the absence of ocean dynamics (Kang et al., 2018a), we find that ocean makes the
469 spatial pattern of tropical climate response dependent on the forcing location. In the SOM
470 configuration, regardless of forcing location, the tropical SST response features a strong

inter-hemispheric contrast, primarily governed by the WES feedback. In the northern tropics, the WES-induced cooling is concomitant with precipitation reduction and hence is partially offset by the shortwave radiation induced warming. In the southern tropics, the WES-induced warming is concomitant with precipitation increase along the SPCZ, overcompensated by the shortwave radiation induced cooling. As a result, the equatorial Pacific cooling response is stronger in the western than the eastern basin, leading to an eastward shift of the rising branch of the Walker circulation. A preferential cooling in the western than the eastern equatorial Pacific is also explained by the blocking effect of the climatological ITCZ (Kang et al., 2020).

The tropical climate response pattern with a large degree of zonal symmetry and strong inter-hemispheric contrast in SOM is altered by spatially distinct ocean heat uptake response. In response to North Asian cooling, the ocean heat uptake increases in the equatorial and the southeastern Pacific, considerably amplifying the cooling response there relative to the SOM experiment. A moderately enhanced zonal SST gradient results in a westward shift of the Walker circulation. In response to European cooling, the ocean heat uptake increase is concentrated in the southeastern basin, strongly amplifying the zonal SST gradient across the equatorial Pacific and thereby intensifying the Walker circulation. As North Asian and European cooling exhibit the tropical Pacific SST and precipitation responses with a high degree of equatorial symmetry, the DOM results are distinct from the corresponding SOM results with a large degree of inter-hemispheric contrast. By contrast, the tropical climate response to North American cooling, with a relatively weaker oceanic compensation in the Indo-Pacific basin, exhibits a considerable similarity in spatial pattern to that in the SOM configuration. A weaker oceanic compensation in response to North American cooling is consistent with White et al., (2018) using a coarse resolution fully coupled model. However, it was outweighed by an even stronger radiative compensation,

causing the atmospheric compensation and the zonal-mean ITCZ shift to be three times weaker in response to North Atlantic perturbation than to North Pacific perturbation. This is in contrast to our results where the radiative cooling over North America induces the largest zonal-mean ITCZ shift associated with the smallest oceanic and radiative compensation. Uncertainty in cloud radiative feedbacks warrants future investigation with different models.

Our experiments clearly demonstrate that a dynamic ocean modifies the spatial structure of the climate response and the exact modification depends on the forcing distribution. While the Walker circulation response to extratropical cooling is shown to be distinct depending on the representation of ocean feedbacks (Kang et al., 2020), this study further reveals the sensitivity to the forcing location. This implies that the geographical distribution of aerosol forcing should be known with precision to properly estimate the aerosol-forced climate change. While we only examine the sensitivity to the zonal location of extratropical radiative cooling, it is imperative to examine the sensitivity to the meridional location as aerosol source regions in Asia have shifted equatorward (Wang and Wen 2021). Furthermore, a future study is warranted that examines the linearity to the forcing sign, with relevance to gradual aerosol reduction in many countries. The responses to radiative heating would be opposite to what is shown here while nonlinearities in climate feedbacks such as those associated with Planck and cloud changes may lead to weaker responses in magnitude (Seo et al. 2014).

References

Deser C, Phillips AS, Simpson IR, et al (2020) Isolating the Evolving Contributions of Anthropogenic Aerosols and Greenhouse Gases: A New CESM1 Large Ensemble Community Resource. Journal of Climate 33:7835–7858. https://doi.org/10.1175/JCLI-D-20-0123.1

Deser C, Tomas RA, Sun L (2015) The Role of Ocean–Atmosphere Coupling in the Zonal-Mean Atmospheric Response to Arctic Sea Ice Loss. Journal of Climate 28:2168–2186. https://doi.org/10.1175/JCLI-D-14-00325.1

Diao C, Xu Y, Xie S-P (2021) Anthropogenic aerosol effects on tropospheric circulation and sea surface temperature (1980–2020): separating the role of zonally asymmetric forcings. Atmos Chem Phys 21:18499–18518. https://doi.org/10.5194/acp-21-18499-2021

Green B, Marshall J, Campin J-M (2019) The 'sticky' ITCZ: ocean-moderated ITCZ shifts. Climate Dynamics 53:1–19. https://doi.org/10.1007/s00382-019-04623-5

Hawcroft M, Haywood JM, Collins M, et al (2017) Southern Ocean albedo, inter-hemispheric energy transports and the double ITCZ: global impacts of biases in a coupled model. Climate Dynamics 48:2279–2295. https://doi.org/10.1007/s00382-016-3205-5

Hirasawa H, Kushner PJ, Sigmond M, et al (2020) Anthropogenic Aerosols Dominate Forced Multidecadal Sahel Precipitation Change through Distinct Atmospheric and Oceanic Drivers. Journal of Climate 33:10187–10204. https://doi.org/10.1175/JCLI-D-19-0829.1

Hoskins BJ, Karoly DJ (1981) The Steady Linear Response of a Spherical Atmosphere to Thermal and Orographic Forcing. Journal of the Atmospheric Sciences 38:1179–1196. https://doi.org/10.1175/1520-0469(1981)038<1179:TSLROA>2.0.CO;2

Hwang Y-T, Frierson DMW, Kang SM (2013) Anthropogenic sulfate aerosol and the southward shift of tropical precipitation in the late 20th century. Geophysical Research Letters 40:2845–2850. https://doi.org/10.1002/grl.50502

Hwang Y-T, Xie S-P, Deser C, Kang SM (2017) Connecting tropical climate change with Southern Ocean heat uptake. Geophysical Research Letters 44:9449–9457. https://doi.org/10.1002/2017GL074972

Kang SM (2020) Extratropical Influence on the Tropical Rainfall Distribution. Current Climate Change Reports 6:24–36. https://doi.org/10.1007/s40641-020-00154-y

Kang SM, Hawcroft M, Xiang B, et al (2019) Extratropical–Tropical Interaction Model Intercomparison Project (Etin-Mip): Protocol and Initial Results. Bulletin of the American Meteorological Society 100:2589–2606. https://doi.org/10.1175/BAMS-D-18-0301.1

Kang SM, Held IM, Frierson DMW, Zhao M (2008) The Response of the ITCZ to Extratropical Thermal Forcing: Idealized Slab-Ocean Experiments with a GCM. J Climate 21:3521–3532. https://doi.org/10.1175/2007JCLI2146.1

555 Kang SM, Held IM, Xie S-P (2014) Contrasting the tropical responses to zonally asymmetric
556 extratropical and tropical thermal forcing. Climate Dynamics 42:2033–2043.
557 https://doi.org/10.1007/s00382-013-1863-0

558 Kang SM, Park K, Hwang Y-T, Hsiao W-T (2018a) Contrasting Tropical Climate Response
559 Pattern to Localized Thermal Forcing Over Different Ocean Basins. Geophysical
560 Research Letters 45:12,544-12,552. https://doi.org/10.1029/2018GL080697

561 Kang SM, Shin Y, Xie S-P (2018b) Extratropical forcing and tropical rainfall distribution:
562 energetics framework and ocean Ekman advection. npj Climate and Atmospheric
563 Science 1:. https://doi.org/10.1038/s41612-017-0004-6

564 Kang SM, Xie S-P, Deser C, Xiang B (2021) Zonal mean and shift modes of historical
565 climate response to evolving aerosol distribution. Science Bulletin
566 S209592732100493X. https://doi.org/10.1016/j.scib.2021.07.013

567 Kang SM, Xie S-P, Shin Y, et al (2020) Walker circulation response to extratropical radiative
568 forcing. Science Advances 6:eabd3021. https://doi.org/10.1126/sciadv.abd3021

569 Kay JE, Wall C, Yettella V, et al (2016) Global Climate Impacts of Fixing the Southern
570 Ocean Shortwave Radiation Bias in the Community Earth System Model (CESM).
571 Journal of Climate 29:21

572 L'Hévéder B, Codron F, Ghil M (2015) Impact of Anomalous Northward Oceanic Heat
573 Transport on Global Climate in a Slab Ocean Setting. J Climate 28:2650–2664.
574 https://doi.org/10.1175/JCLI-D-14-00377.1

575 Ming Y, Ramaswamy V (2009) Nonlinear Climate and Hydrological Responses to Aerosol
576 Effects. Journal of Climate 22:1329–1339. https://doi.org/10.1175/2008JCLI2362.1

577 Samset BH, Lund MT, Bollasina M, et al (2019) Emerging Asian aerosol patterns. Nat
578 Geosci 12:582–584. https://doi.org/10.1038/s41561-019-0424-5

579 Seo J, Kang AM, Frierson DMW (2014) Sensitivity of Intertropical Convergence Zone
580 Movement to the Latitudinal Position of Thermal Forcing. Journal of Climate
581 27:3035–3042. https://doi.org/10.1175/JCLI-D-13-00691.1.
582
583 Shi JR, Kwon YO, Wijffels SE (2022) Two Distinct Modes of Climate Responses to the
584 Anthropogenic Aerosol Forcing Changes. Journal of Climate.
585 https://doi.org/10.1175/JCLI-D-21-0656.1
586
587 Taylor KE, Crucifix M, Braconnot P, et al (2007) Estimating Shortwave Radiative Forcing
588 and Response in Climate Models. Journal of Climate 20:2530–2543.
589 https://doi.org/10.1175/JCLI4143.1

590 Tilmes S, Fasullo J, Lamarque J-F, et al (2013) The hydrological impact of geoengineering in
591 the Geoengineering Model Intercomparison Project (GeoMIP). Journal of
592 Geophysical Research: Atmospheres 118:11,036-11,058.
593 https://doi.org/10.1002/jgrd.50868

Vecchi GA, Delworth T, Gudgel R, et al (2014) On the Seasonal Forecasting of Regional Tropical Cyclone Activity. Journal of Climate 27:7994–8016. https://doi.org/10.1175/JCLI-D-14-00158.1

Wang H, Wen Y-J (2021) Climate response to the spatial and temporal evolutions of anthropogenic aerosol forcing. Climate Dynamics

Wang H, Xie S, Tokinaga H, et al (2016) Detecting cross-equatorial wind change as a fingerprint of climate response to anthropogenic aerosol forcing. Geophysical Research Letters 43:3444–3450. https://doi.org/10.1002/2016GL068521

Wang Y, Jiang JH, Su H (2015) Atmospheric responses to the redistribution of anthropogenic aerosols. Journal of Geophysical Research: Atmospheres 120:9625–9641. https://doi.org/10.1002/2015JD023665

Wang, Y, Jiang JH, Su H, Choi Y-S, Huang L, Guo J, Yung YL (2018) Elucidating the Role of Anthropogenic Aerosols in Arctic Sea Ice Variations. Journal of Climate 31:99–114. https://doi.org/10.1175/JCLI-D-17-0287.1.

White RH, McFarlane AA, Frierson DMW, et al (2018) Tropical Precipitation and Cross-Equatorial Heat Transport in Response to Localized Heating: Basin and Hemisphere Dependence. Geophysical Research Letters 45:11,949-11,958. https://doi.org/10.1029/2018GL078781

Xiang B, Zhao M, Ming Y, et al (2018) Contrasting Impacts of Radiative Forcing in the Southern Ocean versus Southern Tropics on ITCZ Position and Energy Transport in One GFDL Climate Model. Journal of Climate 31:5609–5628. https://doi.org/10.1175/JCLI-D-17-0566.1

Xie S-P, Lu B, Xiang B (2013) Similar spatial patterns of climate responses to aerosol and greenhouse gas changes. Nature Geoscience 6:828–832. https://doi.org/10.1038/ngeo1931

Xie S-P, Philander SGH (1994) A coupled ocean-atmosphere model of relevance to the ITCZ in the eastern Pacific. Tellus A 46:340–350. https://doi.org/10.1034/j.1600-0870.1994.t01-1-00001.x

Yu S, Pritchard MS (2019) A Strong Role for the AMOC in Partitioning Global Energy Transport and Shifting ITCZ Position in Response to Latitudinally Discrete Solar Forcing in CESM1.2. Journal of Climate 32:2207–2226. https://doi.org/10.1175/JCLI-D-18-0360.1

Zhao M, Golaz J-C, Held IM, et al (2018) The GFDL Global Atmosphere and Land Model AM4.0/LM4.0: 1. Simulation Characteristics With Prescribed SSTs. Journal of Advances in Modeling Earth Systems 10:691–734. https://doi.org/10.1002/2017MS001208

Statements and Declarations

Funding

This work was supported by the National Research Foundation of Korea (NRF) grant (NRF-2020K2A9A2A06070756) funded by the Ministry of Science and ICT (MSIT) of South Korea.

Conflicts of interest

The authors declare no competing interests.

Availability of data and material

The regional cooling experiment data in this study can be obtained at the following DOI: https://doi.org/10.5281/zenodo.6355053.

Code availability

Not applicable

Author's contributions

JK, SMK, and SPX developed the idea for this study. SMK, SPX, and BX designed the model experiments. BX performed the model experiments. JK, SMK, and DK conducted the data analysis, with input and feedback from SPX, BX, XTZ, and HW. JK and SMK prepared the manuscript, with contributions from all authors.

Experiment		SOM			DOM		
		NASIA	NAMER	EURO	NASIA	NAMER	EURO
SOM	NASIA	1	0.63	0.86	0.05		
	NAMER	0.74	1	0.72		0.52	
	EURO	0.97	0.77	1			0.19
DOM	NASIA	0.61			1	-0.14	0.04
	NAMER		0.83		0.37	1	-0.11
	EURO			0.60	0.57	0.35	1

Table 1. The pattern correlation coefficients of precipitation response (in green texts) and sea surface temperature response (in red texts) between 30°S-30°N.

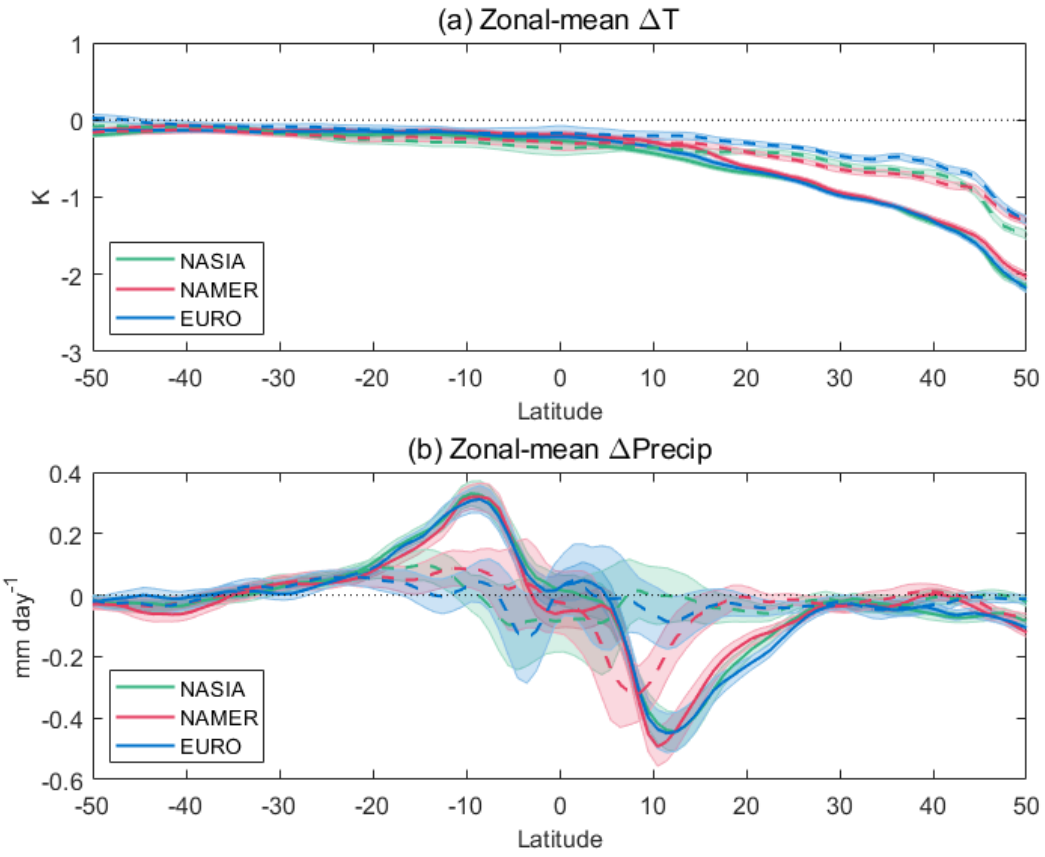

649 Figure 1: The zonal-mean response of (a) surface temperature between 90°S-90°N and (b)
650 precipitation between 30°S-30°N for NASIA (green), NAMER (red), and EURO (blue) in the
651 SOM (solid) and DOM (dashed) experiments. Shading indicates the 95 % significant range
652 based on a two-sided Student t-test.

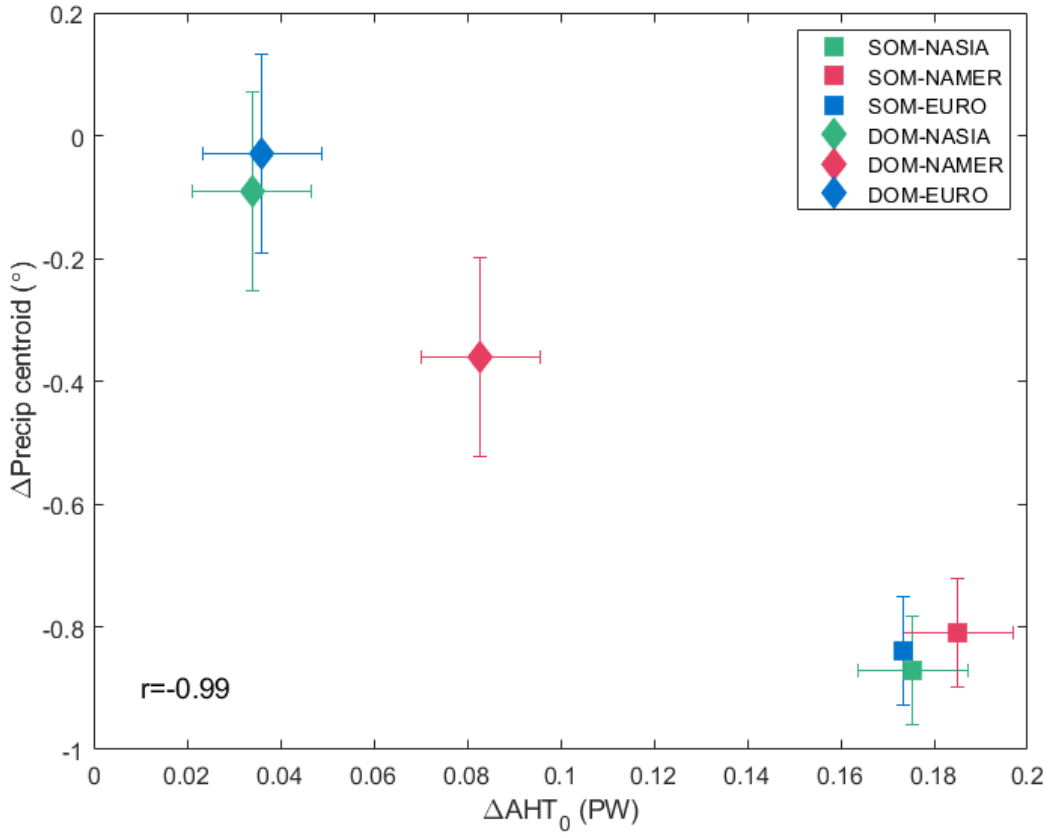

653 Figure 2: Scatterplot of the anomalies in cross-equatorial atmospheric energy transport
654 ΔAHT_0 (in PW) and the precipitation centroid (in °). Error bars indicate the 95 % significant
655 range based on a two-sided Student t-test.
656

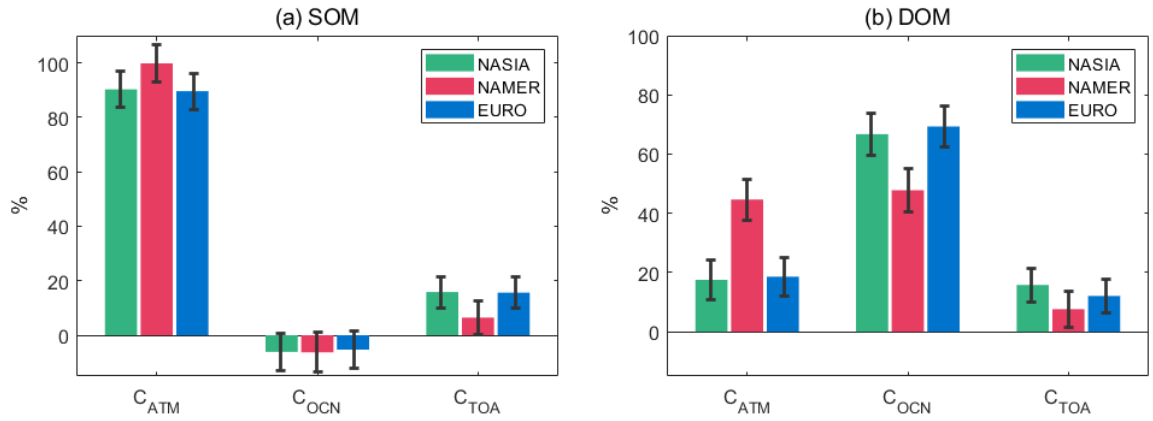

Figure 3: The atmospheric C_{ATM}, oceanic C_{OCN}, and TOA radiative C_{TOA} compensation (%) in NASIA (green), NAMER (red), and EURO (blue) for the (a) SOM and (b) DOM experiments. Error bars indicate the 95 % significant range based on a two-sided Student t-test.

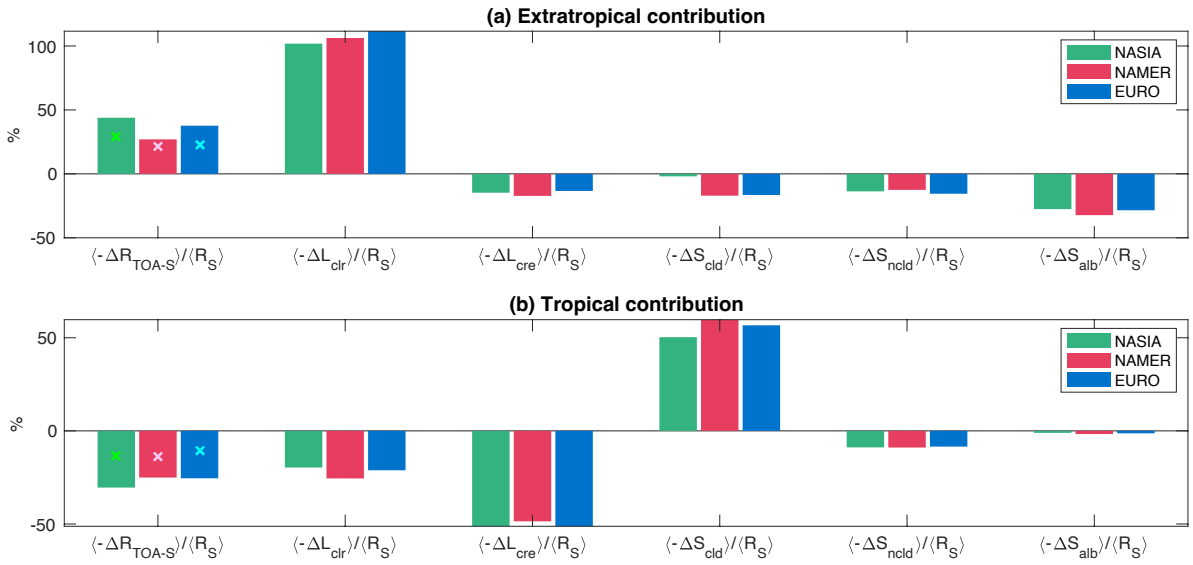

Figure 4: Hemispheric contrast in the TOA radiation response $\langle -\Delta R_{\mathrm{TOA-S}} \rangle$ within (a) the extratropics and (b) the tropics, decomposed into changes in clear-sky longwave flux $\langle -\Delta L_{\mathrm{clr}} \rangle$, longwave cloud radiative effect $\langle -\Delta L_{\mathrm{cre}} \rangle$, shortwave flux due to cloud changes $\langle -\Delta S_{\mathrm{cld}} \rangle$, non-cloud effect changes $\langle -\Delta S_{\mathrm{ncld}} \rangle$, and surface albedo changes $\langle -\Delta S_{\mathrm{alb}} \rangle$, in the SOM experiments. All terms are divided by the forcing term $\langle \Delta R_{\mathrm{S}} \rangle$, being in units of %. The crosses correspond to the respective DOM experiments.

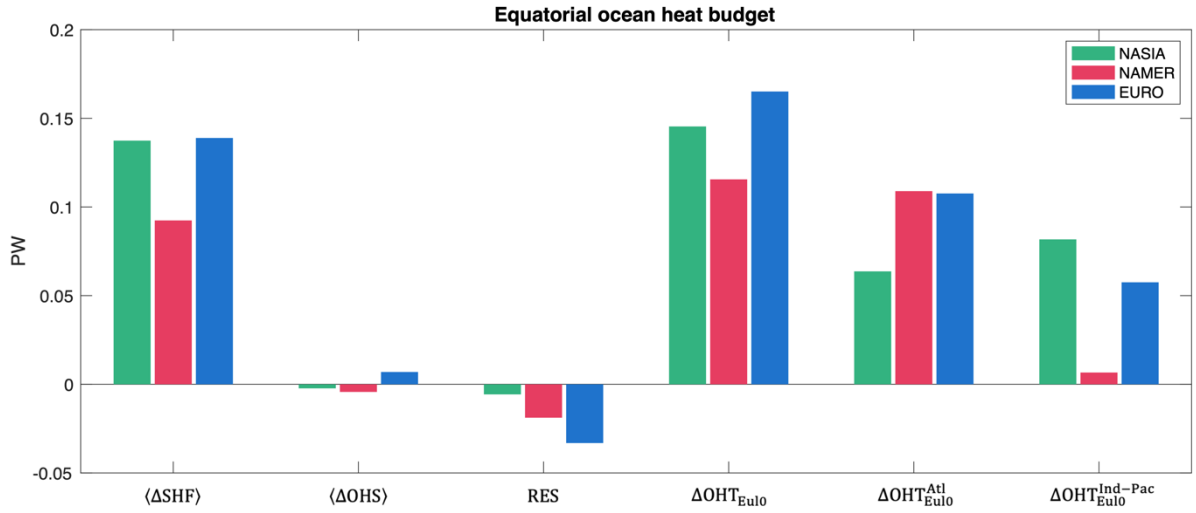

668 Figure 5: Ocean heat budget on the equator for the DOM experiments. Hemispheric contrast
669 in anomalous net downward surface heat flux ⟨ΔSHF⟩ is decomposed into hemispheric
670 contrast in anomalous ocean heat storage ⟨ΔOHS⟩, anomalous cross-equatorial ocean heat
671 transport by Eulerian-mean flow $\Delta\mathrm{OHT}_{\mathrm{Eul0}}$, and the residual RES. The Eulerian-mean ocean
672 heat transport is calculated separately for the Atlantic ($\Delta\mathrm{OHT}^{\mathrm{Atl}}_{\mathrm{Eul0}}$) and Indo-Pacific
673 ($\Delta\mathrm{OHT}^{\mathrm{Ind-Pac}}_{\mathrm{Eul0}}$) sectors.

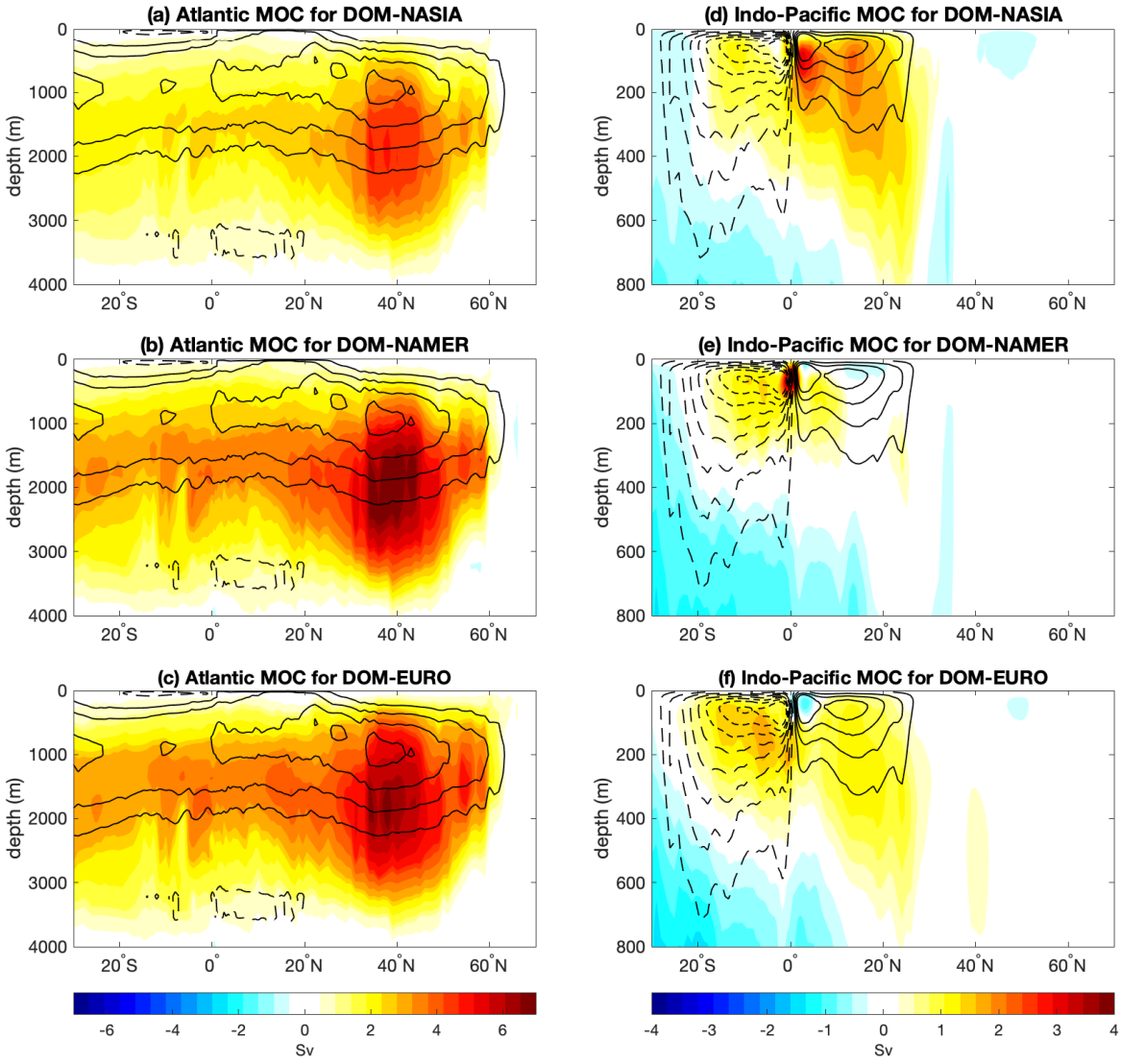

674 Figure 6: Ocean meridional overturning circulation anomalies in the (left) Atlantic and (right)
675 Indo-Pacific sectors. The contours show the control climatology (interval = 5 Sv). Positive
676 values (red shading and solid contours) indicate a clockwise circulation and negative values
677 (blue shading and dashed contours) indicate a counter-clockwise circulation.

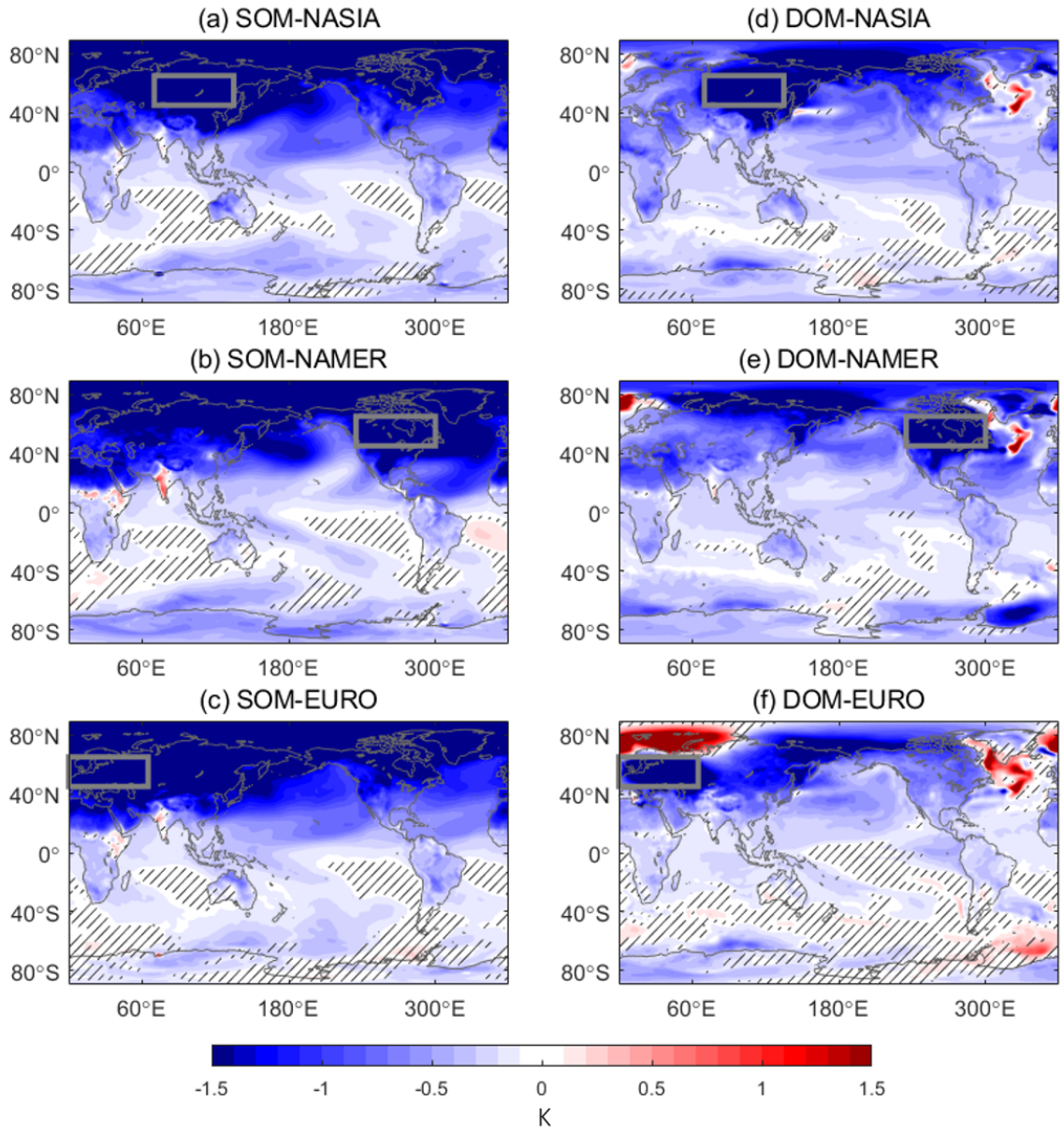

678 Figure 7: Surface temperature response for the SOM (left) and DOM (right) experiments.
679 Thick gray rectangles indicate the forcing location for (a,d) NASIA, (b,e) NAMER, and (c,f)
680 EURO. Hatching indicates where the response is not statistically significant at the 95%
681 confidence level using a two-sided t-test.

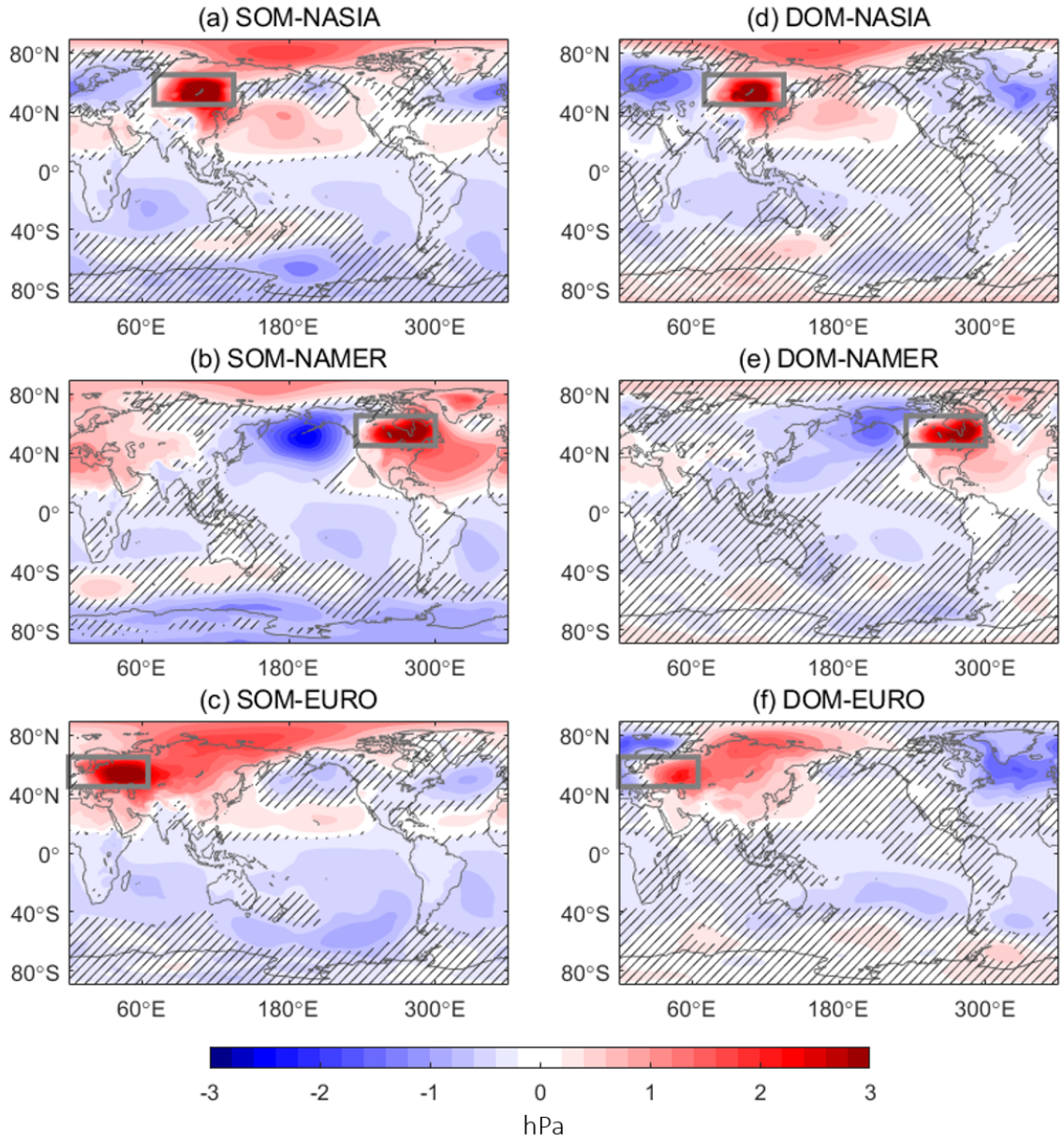

682 Figure 8: Similar to Fig. 7 but for the sea level pressure response.
683
684
685

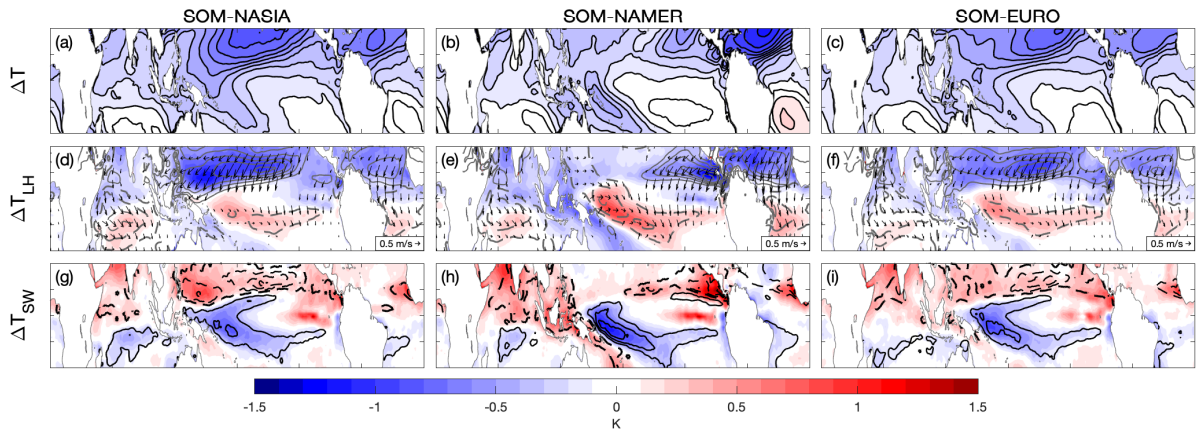

Figure 9: **Tropical SST response attribution in SOM experiments.** (a,b,c) The SST response (shading; interval = 0.1 K) and the linear sum of the five decomposed components in Eq. (2) (contours; interval = 0.1 K). (d,e,f) The SST response due to $\Delta Q_{\mathrm{LH,others}}$ (shading; interval = 0.1 K), the reference level wind speed changes (positive in solid and negative in dashed; interval = 0.2 m s^{-1}), and the wind velocity response that are statistically significant at the 95% confidence level using a two-sided *t*-test (vectors). (g,h,i) The SST response due to ΔQ_{SW} (shading; interval = 0.1 K) and the precipitation response (positive in solid and negative in dashed; interval = 0.4 mm day^{-1}). Results from SOM-NASIA (left), SOM-NAMER (middle), and SOM-EURO (right).

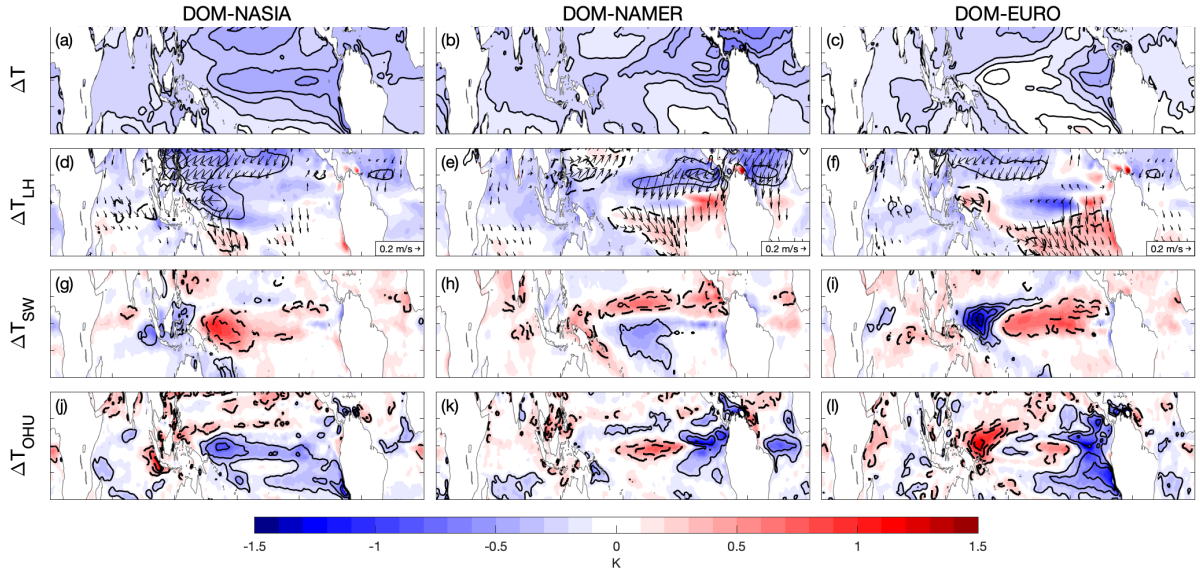

Figure 10: **Tropical SST response attribution in DOM experiments.** (a,b,c) The SST response (shading; interval = 0.1 K) and the linear sum of the decomposed components in Eq. (2) (contours; interval = 0.1 K). (d,e,f) The SST response due to $\Delta Q_{\mathrm{LH,others}}$ (shading; interval = 0.1 K) and the surface wind speed changes (positive in solid and negative in dashed; interval = 0.2 m s^{-1}). (g,h,i) The SST response due to ΔQ_{SW} (shading; interval = 0.1 K), the precipitation response (positive in solid and negative in dashed; interval = 0.4 mm day^{-1}), and the reference level wind response that are statistically significant at the 95% confidence level using a two-sided *t*-test (vectors). (j,k,l) The SST response due to ΔOHU (shading; interval = 0.1 K) and the net surface heat flux changes (downward in solid and upward in dashed; interval = 2 W m^{-2}). Results from DOM-NASIA (left), DOM-NAMER (middle), and DOM-EURO (right).

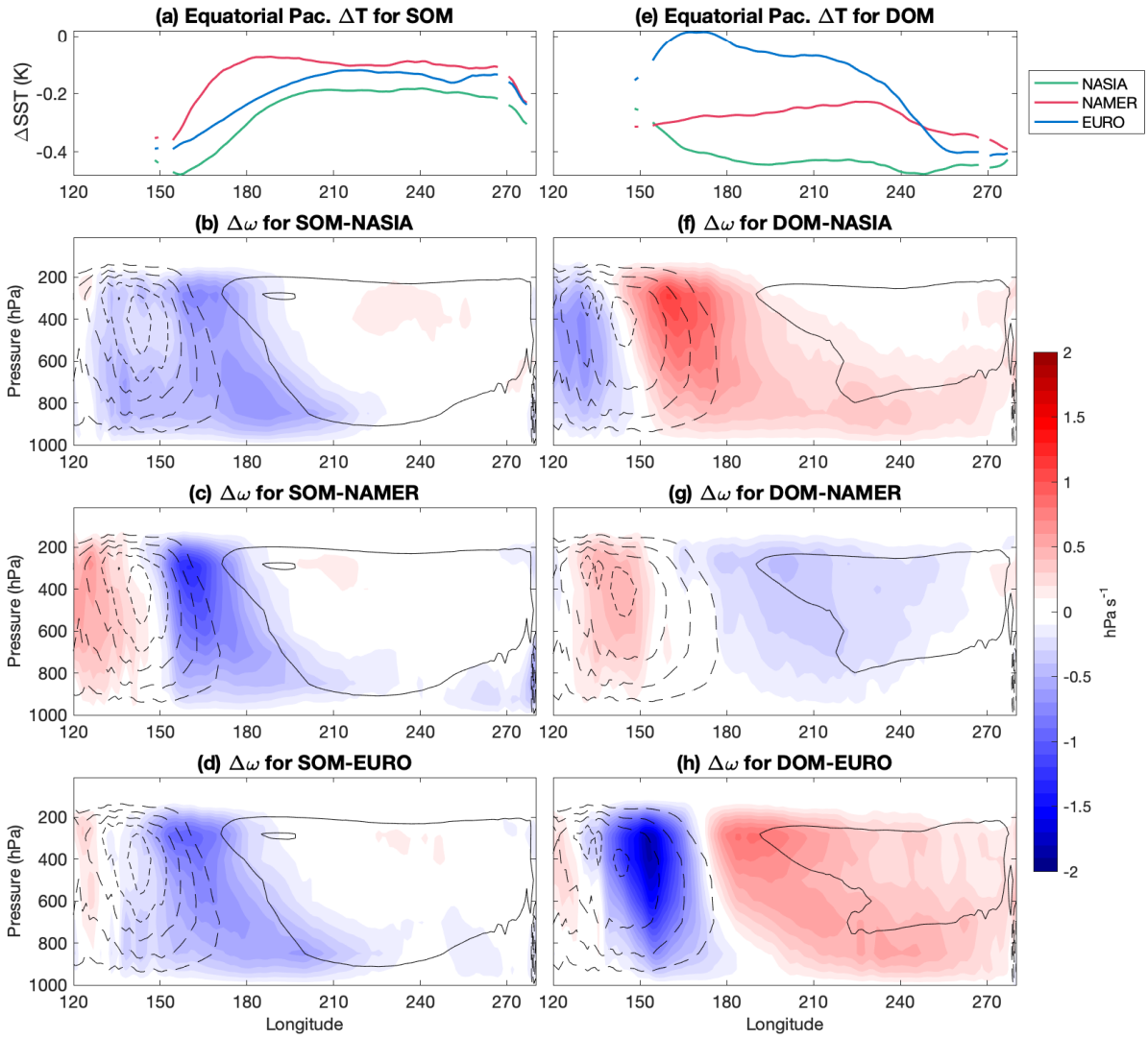

Figure 11: The 5°S-5°N averaged (a) SST response and (b-d) pressure velocity response in shading (hPa s^{-1}) and the control climatology in contours (negative in dashed and positive in solid, interval = 2 hPa s^{-1}) over the Pacific basin in the SOM experiments. (Right) Similar to left but for the DOM experiments.